Role of hydrodynamic and acoustic pressures in trailing-edge noise using numerical and analytical approaches

Donghun Kang and Seongkyu Lee*
Department of Mechanical and Aerospace Engineering, University of California, Davis, California 95616, USA

(Received 3 August 2024; accepted 10 March 2025; published 27 March 2025)

This study employs wall-resolved large-eddy simulation of a NACA 0012 airfoil at a Reynolds number of 400 000, a Mach number of 0.058, and zero incidence angle to investigate the fundamental mechanisms governing trailing-edge noise generation and propagation within turbulent boundary-layer flows. It utilizes wave-number-frequency decomposition and Amiet's trailing-edge noise theory to separate total pressure into two distinct components: hydrodynamic (incident) pressure and acoustic (scattered) pressure. The findings reveal that hydrodynamic pressure consists of turbulent coherent structures characterized by high-energy spectra, but they act as nonpropagating sources due to destructive interference within the streamwise correlation length. In contrast, acoustic pressure exhibits an in-phase nature that facilitates efficient sound propagation. The roles of incident and scattered pressures in Amiet's theory are compared with hydrodynamic and acoustic pressures obtained from a numerical simulation, revealing similarities in magnitude and directivity patterns.

DOI: 10.1103/PhysRevFluids.10.034609

I. INTRODUCTION

The amplification of noise radiation is well established when noise sources are near solid boundaries such as airfoil surfaces [1,2]. Brooks *et al.* [3] identified five primary mechanisms of airfoil self-noise, including turbulent boundary-layer trailing-edge noise, laminar boundary-layer instability noise, trailing-edge bluntness noise, separation-stall noise, and tip vortex noise. Among these, turbulent boundary-layer trailing-edge noise is especially important in various engineering applications, ranging from airframe configurations to rotating blades. The practical examples include advanced air mobility aircraft, wind turbines, and marine propellers. A comprehensive review of analytical, experimental, and numerical studies related to trailing-edge noise can be found in Ref. [4].

There have been significant strides in developing theories related to turbulent boundary-layer trailing-edge noise over several decades, with foundational works starting as early as the 1970s [5–9]. For example, Ffowcs Williams and Hall [5] delved into the scattering effect of turbulence near a sharp edge. They integrated the rigid half-plane Green's function with volumetric sources that depict wake velocity statistics in Lighthill's equations [10]. Howe [9] further contributed with an asymptotic theory, wherein the scattering is characterized using the Wiener-Hopf method iteratively, with a dipole source defined by the wall pressure spectrum and spanwise correlation length.

In addition, Amiet [6–8] derived an aeroacoustic transfer function, based on the Schwarzschild solution to handle the scattering effect. Amiet combined this aeroacoustic transfer function with

*Contact author: skulee@ucdavis.edu

acoustic sources near the trailing edge such as spanwise correlation length and the wall pressure spectrum to determine the acoustic power spectral density. However, the theory rests on several assumptions, such as the exponential decay of incident pressure from the trailing edge to the leading edge, frozen turbulence [11], an infinitely long span, and a flat plate at zero incidence. Yet, despite such oversimplifications, the introduction of an advanced empirical wall pressure spectrum model [12] to Amiet's model has led to favorable outcomes for airfoil and rotor broadband noise predictions [13–15]. This groundwork has facilitated successive refinements such as factoring in leading-edge backscattering [16] and accounting for the airfoil camber and thickness [17]. In Amiet's theory, it is important to note that both the hydrodynamic incident pressure and the acoustic scattering pressure serve as the sources of far-field noise. While several researchers [18–21] as well as Amiet himself [8] have delved into examining the relative contributions of these pressures, the intricate physical dynamics underlying how each pressure distinctly contributes to the far-field noise warrants deeper exploration. This is at the forefront of our investigation in this paper.

In numerical simulations, one can independently compute noise originating from both the incident and scattered pressures in conjunction with acoustic scattering solvers, such as the finite element method (FEM) or the boundary element method (BEM), along with an acoustic analogy. Oberai *et al.* [18] addressed the computation of trailing-edge noise through the variational formulation of Lighthill's acoustic analogies [10] using the FEM. They distinguished sound sources into incident and scattered fields. The incident field was either modeled as a basic quadrupole source or derived from Lighthill's turbulence tensor in free space. Conversely, the scattered field was computed by subtracting the incident contribution from the total pressure. Their observations revealed that the scattered component influences the directional attributes of the total pressure throughout the entire frequency spectrum. They noted that the resultant scattered sound retains a dipole pattern at low frequencies, corroborated by Curle's solution [1]. Moreover, the peak noise level in terms of directivity tends to lean upstream as the frequency increases. At high frequencies, additional lobes emerge in the dipole pattern due to scattering by wavelengths smaller than the airfoil chord length. Consistent findings were reported by Martínez-Lera *et al.* [20,21]. They used the FEM along with Lighthill's formulation, and their results indicated that the primary noise source emanating from the airfoil results from the scattering effect, with the incident field playing a minimal role. Khalighi *et al.* [19] used the BEM to solve Lighthill's equation in the presence of a body. Their most salient observation is the dominance of the scattering effect at high frequencies, contrasting it with sounds solely emanating from hydrodynamic sources on the wall.

In compressible large-eddy simulations (LESs), it is more challenging to separate the incident pressure and the scattered pressure since the flow solutions inherently encompass both hydrodynamic pressure fluctuations and scattered acoustic pressures on the wall. Various methodologies exist for distinguishing between these pressures [22–25]. The essence of these methods lies in leveraging the disparity in phase speeds between hydrodynamic and acoustic pressures. Shubham *et al.* [26] utilized the wave-number-frequency decomposition technique to distinguish hydrodynamic pressures from acoustic pressures in the study of airfoil noise. Their analysis identified the cause of the pronounced high-frequency broadband humps observed at high Mach numbers. Specifically, they attributed the amplification of acoustic pressures to the presence of a separation bubble near the leading edge.

A key advantage of employing LES lies in its capability to generate extensive datasets. These datasets can be seamlessly integrated with data-driven postprocessing routines, enabling a comprehensive analysis of the characteristics of each pressure component. For instance, dynamic mode decomposition (DMD) [27] has been employed to analyze pressure waves generated by both dipole and quadrupole sources around the airfoil at specific frequencies [28]. Building on modal analyses, Sanjose *et al.* [29] elucidated the aeroacoustic mechanisms associated with trailing-edge noise by identifying the diffraction of coherent structures at the trailing edge. Concurrently, other studies [30,31] have emphasized the role of spanwise-coherent structures in trailing-edge noise, highlighting that these two-dimensional disturbances consistently meet the conditions necessary for sound generation. Sano *et al.* [30] substantiated this hypothesis through flow-acoustic correlation

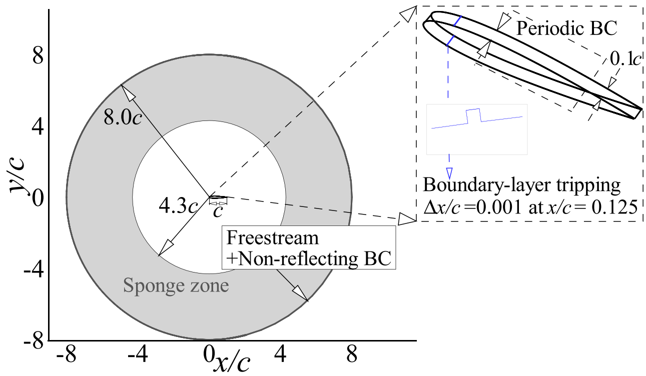

FIG. 1. Boundary conditions over the computational domain.

and spectral proper orthogonal decomposition (SPOD) [32] analyses. Furthermore, the recently developed cross-spectrum analysis [33] provides a novel approach for examining the impact of decomposed pressure components, offering additional insights beyond previous methodologies.

Theoretical and numerical investigations have substantially advanced our understanding of the generation and propagation mechanisms of trailing-edge noise. Nevertheless, the intricate contributions of hydrodynamic and acoustic pressures to far-field noise remain inadequately elucidated. This study seeks to address this knowledge gap through a multifaceted approach combining compressible LES simulations, wave-number-frequency Fourier filtering based on phase speed, cross-correlation and phase analyses, and the application of the FW-H acoustic analogy [34] to segmented airfoil surfaces.

Furthermore, we revisit Amiet's theory, contrasting the incident and scattered fields within an analytical framework against numerical results derived from LES. This comparison evaluates the efficacy and precision of Amiet's model in capturing the roles of incident and scattered pressures. Ultimately, this paper aims to illuminate the underlying physics governing trailing-edge noise generation and propagation through comprehensive pressure decomposition, providing a deeper insight into these complex aeroacoustic phenomena.

II. METHODOLOGY

A. Computational domain and boundary conditions

The computational domain and boundary conditions surrounding a NACA 0012 airfoil with a blunt trailing-edge configuration are illustrated in Fig. 1. The trailing-edge bluntness, denoted as h_{TE}/δ^*, or the ratio of the trailing-edge thickness (h_{TE}) to the displacement thickness (δ^*) calculated at $x/c \approx 0.99$, is determined to be 0.5. We have employed an O-type two-dimensional computational domain with a radius of $8.0c$, where c represents the airfoil chord length. This domain extends by $0.1c$ in the spanwise direction, and periodic boundary conditions are applied to the two O-type planes to facilitate three-dimensional simulations. Unlike massively separated flows [35,36], this spanwise size was found to be sufficient for turbulent noise sources that exponentially decay under current flow regimes [37]. The airfoil itself is equipped with a no-slip wall boundary condition, while the freestream boundary encompasses the outer edge of the computational domain. To mitigate acoustic perturbations within the finite computational domain, a nonreflecting boundary condition is implemented alongside the freestream boundary. Additionally, a sponge zone is introduced, consisting of a concentric circle with a radius spanning from $4.3c$ to $8.0c$. This sponge zone is designed to dampen acoustic disturbances. To induce turbulent flows downstream, a boundary layer is tripped using a squared trip dot positioned at 12.5% of the airfoil's leading edge on both sides.

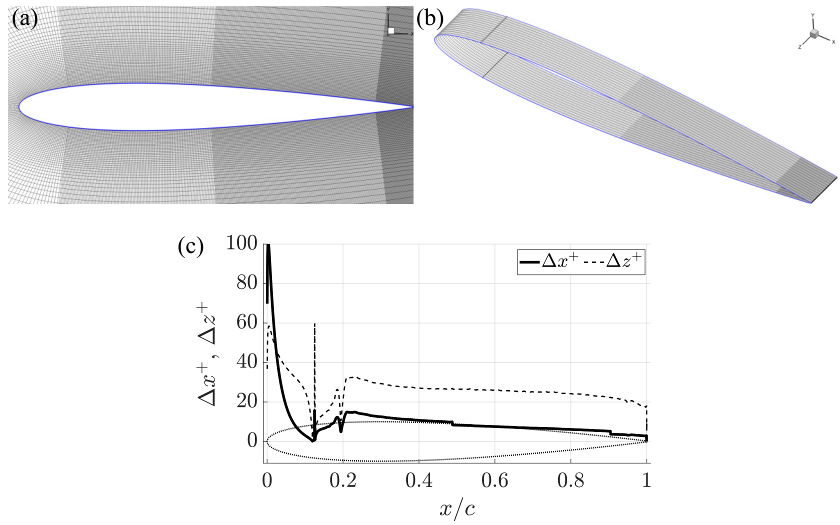

FIG. 2. Structured mesh topology: (a) airfoil near-wall region, (b) surface on the airfoil (for clarity, the meshes are displayed for every fourth grid line), and (c) streamwise and spanwise grid spacing in wall unit.

B. Grid topology

Figure 2 provides an overview of the grid topology within the computational domain. The structured meshes are visible near the airfoil [Fig. 2(a)] and on the wall [Fig. 2(b)]. The grid dimensions are specified as $N_x \times N_y \times N_z = 4308 \times 323 \times 65$ in the streamwise, normal, and spanwise directions, respectively, resulting in an approximate total cell count of 90 million. Notably, the grid resolution is uniform on both sides of the airfoil. Mesh refinement is evident near the trailing edge, a crucial aspect for accurately resolving acoustic sources and scattering at this location. To quantify the grid size, it is depicted in Fig. 2(c) as grid spacing normalized by the viscous lengthscale, denoted as $\Delta x^+ = \Delta x u_\tau/\nu$ and $\Delta z^+ = \Delta z u_\tau/\nu$. Here, u_τ represents the friction velocity, and ν denotes the kinematic viscosity. The results indicate that Δx^+ remains below 20, while Δz^+ is less than 40 around the stair strip, where the laminar-to-turbulent transition initiates. Additionally, the average value of the first cell height y^+ along the airfoil surface is less than 0.5. Therefore, the current grid resolution aligns with the criteria for grid size in wall-resolved LES as outlined by Georgiadis *et al.* [38].

C. Governing equations and numerical methods

The equations governing the large-scale motions of compressible flows can be formulated using Favre-filtered quantities, as outlined in previous studies [39–41]. In the following, the operator symbols $\bar{\cdot}$ and $\tilde{\cdot}$ are employed to denote the Reynolds and Favre averages, respectively, following the notation introduced by Favre [42]. These equations encompass the continuity, momentum, and total energy equations, which are expressed as follows:

$$\frac{\partial \bar{\rho}}{\partial t} + \frac{\partial}{\partial x_j}(\bar{\rho}\tilde{v}_j) = 0, \tag{1}$$

$$\frac{\partial \bar{\rho}\tilde{v}_i}{\partial t} + \frac{\partial}{\partial x_j}(\bar{\rho}\tilde{v}_j\tilde{v}_i) = -\frac{\partial \bar{p}}{\partial x_i} + \frac{\partial \tilde{\sigma}_{ij}}{\partial x_j} - \frac{\partial \tau_{ij}^{\mathrm{sgs}}}{\partial x_j}, \tag{2}$$

$$\frac{\partial \bar{\rho}\tilde{E}}{\partial t} + \frac{\partial}{\partial x_j}(\bar{\rho}\tilde{v}_j\tilde{H}) = \frac{\partial}{\partial x_j}(\tilde{v}_i\tilde{\sigma}_{ij}) + \frac{\partial}{\partial x_j}\left(\tilde{k}\frac{\partial \tilde{T}}{\partial x_j}\right) - \frac{\partial}{\partial x_j}\left(\tilde{v}_i\tau_{ij}^{\mathrm{sgs}}\right) - \frac{\partial q_j^{\mathrm{sgs}}}{\partial x_j}, \tag{3}$$

where $\bar{\rho}$, $\tilde{v}_i$, $\tilde{E}$, $\tilde{H}$, $\tilde{T}$, $\tilde{k}$ are the filtered density, filtered velocity components in the ith direction, filtered total energy $\tilde{e} + \tilde{v}_k \cdot \tilde{v}_k/2$, filtered total enthalpy $\tilde{E} + \bar{p}/\bar{\rho}$, filtered temperature, and filtered thermal conductivity. Here, $\tilde{e}$, $\bar{p}$ are the filtered internal energy and filtered pressure, respectively. τ_{ij}^{sgs} is the Favre-averaged subgrid-scale (SGS) stress tensor denoted as $\bar{\rho}(\widetilde{v_i v_j} - \tilde{v}_i\tilde{v}_j)$, while q_j^{sgs} is the SGS heat flux denoted as $\bar{\rho}(\widetilde{e v_j} - \tilde{e}\tilde{v}_j)$. $\tilde{S}_{ij}$ denotes the rate of strain tensor of the resolved flow field, which is defined as

$$\tilde{S}_{ij} = \frac{1}{2}\left(\frac{\partial \tilde{v}_i}{\partial x_j} + \frac{\partial \tilde{v}_j}{\partial x_i}\right). \tag{4}$$

$\tilde{\sigma}_{ij}$ is the shear-stress tensor of the resolved flow field, which is defined as

$$\tilde{\sigma}_{ij} = 2\tilde{\mu}\left(\tilde{S}_{ij} - \tfrac{1}{3}\tilde{S}_{kk}\delta_{ij}\right), \tag{5}$$

where $\tilde{\mu}$, δ_{ij} are the filtered dynamic viscosity and Kronecker symbol, respectively. Both SGS components, τ_{ij}^{sgs} and q_j^{sgs}, must be modeled, the former being determined based on the deviatoric stress tensor for the eddy viscosity assumption:

$$\tau_{ij}^{\text{sgs}} - \tfrac{1}{3}\tau_{kk}^{\text{sgs}}\delta_{ij} = -2\bar{\rho}\nu_T\left(\tilde{S}_{ij} - \tfrac{1}{3}\tilde{S}_{kk}\delta_{ij}\right), \tag{6}$$

where ν_T stands for the turbulent eddy viscosity. This relates the SGS stress tensor to the turbulent eddy viscosity and the rate of strain tensor. Likewise, the SGS heat flux q_j^{sgs} can be associated with the turbulent eddy viscosity as $q_j^{\text{sgs}} = -\frac{\bar{\rho}\nu_T C_p}{\text{Pr}_t}\frac{\partial \tilde{T}}{\partial x_j}$, where C_p is the specific heat at constant pressure, and Pr_t is the SGS turbulent Prandtl number equal to 0.85, which is the ratio of the turbulent eddy viscosity to the thermal diffusivity, thus being determined by calculating ν_T [39]. In this paper, the turbulent eddy viscosity ν_T is determined by the wall-adapting local eddy-viscosity (WALE) [43] model defined as

$$\nu_T = (C_w\Delta)^2\frac{\left(S_{ij}^d S_{ij}^d\right)^{3/2}}{(\tilde{S}_{ij}\tilde{S}_{ij})^{5/2} + \left(S_{ij}^d S_{ij}^d\right)^{5/4}}, \tag{7}$$

where C_w is specified as 0.325, Δ is the filter width defined as $(\Delta_x, \Delta_y, \Delta_z)^{1/3}$, and S_{ij}^d is defined as

$$S_{ij}^d = \frac{1}{2}\left(\left(\frac{\partial \tilde{v}_i}{\partial x_j}\right)^2 + \left(\frac{\partial \tilde{v}_j}{\partial x_i}\right)^2\right) - \frac{1}{3}\delta_{ij}\left(\frac{\partial \tilde{v}_k}{\partial x_k}\right)^2. \tag{8}$$

In our simulations of compressible turbulent flows, we employ the rhoPimpleFoam solver, which represents a density-based PIMPLE (Pressure Implicit with the Splitting of Operator combined with Semi-Implicit Method for Pressure-Linked Equations) algorithm [44]. The computational domain is discretized using the finite volume method. Spatial variables are discretized with second-order accuracy, utilizing the Gauss linear scheme, while temporal variables are discretized using the backward-differencing scheme. The initial flow field for LESs is derived from a steady-state Reynolds-averaged Navier-Stokes (RANS) simulation. In this RANS simulation, we employ the k-ω shear stress transport model proposed by Menter [45] as a closure model. To ensure temporal accuracy, time-accurate simulations are conducted with a nondimensional time step denoted as τ^*, which is selected as 1.133×10^{-3} and expressed as $\Delta t c_o/l$. Here, Δt, c_o, and l represent the physical time step, speed of sound, and characteristic length, respectively. The simulations progress in time while maintaining a Courant-Friedrichs-Lewy (CFL) number of less than 0.9. The total duration of the LES corresponds to 20 airfoil flow-through times (FTT). Spectral analyses are conducted using numerical data collected at intervals of 1/3000 FTT during the final 10 FTT, where flow statistics have reached convergence.

D. Wave-number-frequency decomposition

The wave-number-frequency analysis is represented in the form of a multidimensional Fourier transform. This multidimensional spectrum can be expressed as follows:

$$\mathbf{P}(f,k) = \int_{-\infty}^{\infty}\int_{-\infty}^{\infty} p(t,x)\mathrm{e}^{-\mathrm{i}(2\pi f t - kx)}\,\mathrm{d}t\,\mathrm{d}x, \tag{9}$$

where k represents the wave number, f denotes the frequency, and t stands for time. Specifically, only the streamwise wave number is considered, simplifying the identification of various wave modes based on their propagation direction and speed. This approach enables the isolation of specific wave modes through a filtering process, allowing for the detection of a single-mode wave [26]. Time-accurate pressure data are collected from probes distributed evenly on both the upper and lower sides of the airfoil. The wave-number resolution, denoted as Δk, is determined as $\Delta k = 3.33\ \mathrm{m}^{-1}$, which is calculated using the formula $\Delta k = 1/(N\mathrm{d}x)$, where N represents the number of probes, and $\mathrm{d}x$ is the distance between neighboring probes. Wave number, in this context, is defined as the number of complete waves within a unit distance, with units of m^{-1}. Fourier coefficients in the wave-number-frequency domain are subjected to filtering using the following relationship:

$$\mathbf{P_Y}(f,k) = \mathbf{P}(f,k)\hat{Y}(f,k), \tag{10}$$

$$\hat{Y}(f,k) = \begin{cases} 1, & f_{\text{lower band}} \leqslant f \leqslant f_{\text{upper band}}, \\ 0, & f > f_{\text{upper band}}, \\ 0, & f < f_{\text{lower band}}, \end{cases} \tag{11}$$

where $\mathbf{P_Y}(f,k)$ represents the filtered Fourier coefficient, while $\hat{Y}(f,k)$ stands for the filtering coefficient, taking values of either 0 or 1. The lower and upper bands of the filtering coefficient delineate the threshold range, which is determined by the phase velocities of convective velocity $U_c \approx 0.8U_\infty$ and the speed of sound c_o. The acoustic-wave mode can be further decomposed into downstream and upstream waves, resulting in the identification of three distinct pressure waves upon decomposition. These are as follows: hydrodynamic pressure (p_{hy}), which travels along the wall at the convective velocity U_c, downstream acoustic pressure (p_{ac}^{+}), propagating at a speed of approximately $U_c + c_o$, and upstream acoustic pressure (p_{ac}^{-}), propagating in the opposite direction to the freestream, approximately at $U_c - c_o$. The filtered pressure spectra are then transformed back to the time domain by applying the inverse Fourier transform denoted as $\mathcal{F}^{-1}[:]$,

$$p_Y(t,x) = \mathcal{F}^{-1}[\mathbf{P_Y}(f,k)]. \tag{12}$$

The filtering process is repeated until three wave modes of the pressure are obtained:

$$p_Y(t,x) = p_{\mathrm{hy}} + p_{\mathrm{ac}}^{+} + p_{\mathrm{ac}}^{-}. \tag{13}$$

E. Ffowcs Williams-Hawkings acoustic analogy

The calculation of sound radiation is carried out using Farassat's Formulation 1A [46], which involves solving the integral formulation of the Ffowcs Williams-Hawkings (FW-H) equation [34]. This computational process is implemented in the psu-wopwop code [47,48]. Pressure fluctuations occurring on the surface of the airfoil within the spanwise length of $0.1c$ are extracted to calculate the loading noise. In the case of low-speed Mach numbers, the analysis excludes considerations for thickness noise and the quadrupole source term within the FW-H equation. The sets of equations representing Farassat's Formulation 1A for loading noise are as follows:

$$p'(\mathbf{x},t) = p'_L(\mathbf{x},t), \tag{14}$$

$$4\pi p'_L(\mathbf{x},t) = \frac{1}{c}\int_{f=0}\left[\frac{\dot{l}_r}{r|1-M_r|^2}\right]_{\text{ret}} \mathrm{d}S + \int_{f=0}\left[\frac{l_r - l_M}{r^2|1-M_r|^2}\right]_{\text{ret}} \mathrm{d}S$$
$$+ \frac{1}{c}\int_{f=0}\left[\frac{l_r(r\dot{M}_r + c(M_r - M^2))}{r^2|1-M_r|^3}\right]_{\text{ret}} \mathrm{d}S, \tag{15}$$

where M_r, $1/|1-M_r|$, r, $\dot{l}_r$, $f=0$ are the source Mach number in the sound radiation direction, the Doppler amplification factor, the relative distance between the source and an observer, the rate of change of the surface pressure, and the acoustic data surface, respectively. The integrands are evaluated at the retarded time. It is important to note that the receivers move at the same speed as the airfoil within a stationary medium. This scenario is analogous to an acoustic field within a wind tunnel, where the airfoil and observers are stationary while the medium—the airflow—remains in motion.

F. Amiet's trailing-edge noise theory

Amiet [6–8] developed a model for trailing-edge noise in uniform flow, considering a flat plate or a thin airfoil within a source coordinate system (X, Y, Z). Each axis coordinate is normalized by half the chord length, denoted as b, oriented in the streamwise, spanwise, and wall-normal directions. The airfoil streamwise extends from -2 to 0, and the origin of the source coordinate is at the trailing edge. The incident pressure field upstream of the trailing edge in the frequency domain is represented as follows:

$$g_o(X,Y,\omega) = \mathrm{e}^{-\mathrm{i}(\alpha\bar{K}X + \bar{K}_2 Y) + \epsilon\alpha\bar{K}X}, \tag{16}$$

where $\alpha = U_\infty/U_c$, $\bar{K} = Kb$ with $K = \omega/U_\infty$, $\bar{K}_2 = K_2 b$ with $K_2 = \omega y/(c_o S_o)$. Here, S_0 is $\sqrt{x_1^2 + \beta^2(x_2^2 + x_3^2)}$ for the observer located at (x_1, x_2, x_3), $\beta^2 = 1 - M^2$, $M = U_\infty/c_o$, c_o is the speed of sound, and ω is the angular frequency. The parameters U_∞ and U_c are the freestream velocity and turbulence convection velocity, the latter approximately being $0.8U_\infty$, consistent with the wave-number-frequency decomposition (Sec. II D). In this paper, $K_2 = 0$. The parameter ϵ is used as an exponential convergence factor, designed to maintain the incident pressure at the trailing edge while causing it to exponentially diminish towards the leading edge [8,49]. In this context, the value of the exponential convergence factor ϵ is set to 0.01. Importantly, the ultimate solution produced by Amiet's model is not significantly affected by the specific choice of this value. The scattered pressure is determined using Schwarzschild's solution, which satisfies the Kutta condition, and it is expressed as follows:

$$g_s(X,Y,\omega) = \mathrm{e}^{-\mathrm{i}\alpha\bar{K}X}[(1+\mathrm{i})E^*(-[\alpha\bar{K} + \bar{\kappa} + M\bar{\mu}]X) - 1], \tag{17}$$

where E^* is the complex error function defined as

$$E^*(x) = \int_0^x \frac{\mathrm{e}^{-\mathrm{i}t}}{\sqrt{2\pi t}}\mathrm{d}t = C_2(x) - \mathrm{i}S_2(x). \tag{18}$$

In this equation, C_2 and S_2 are Fresnel integrals [50]. Here, $\bar{\kappa}^2 = \bar{\mu}^2 - \frac{\bar{K}_2^2}{\beta^2}$ with $\bar{\mu} = \bar{K}M/\beta^2$.

1. *Aeroacoustic transfer functions*

The aeroacoustic transfer function is derived by integrating the incident pressure and the scattered pressure from the leading edge to the trailing edge, utilizing the following equation:

$$\mathcal{L}(\vec{x},\omega) = \int_{-2}^{0} g(X,Y,\omega)\mathrm{e}^{-\mathrm{i}\bar{\mu}(M - \frac{x_1}{S_0})X}\,\mathrm{d}X, \tag{19}$$

where $\vec{x}$ denotes the vector of the observer coordinate system.

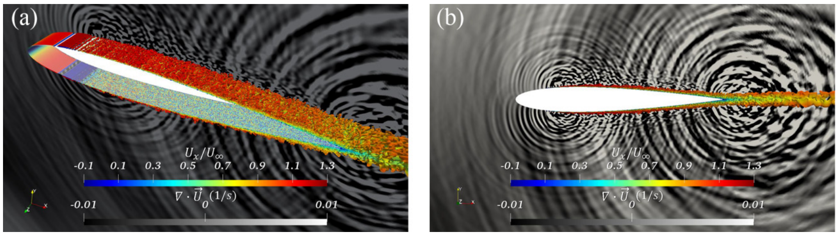

FIG. 3. Normalized Q-criterion ($Qc^2/U_\infty^2 = 10$) colored with the streamwise velocity component (U_x/U_∞) with the dilatation field ($\nabla \cdot \vec{U}$) in the background: (a) isometric view and (b) plane view normal to the spanwise direction.

The aeroacoustic transfer function for the incident pressure is given by

$$\mathcal{L}_o(\vec{x}, \omega) = -\frac{1}{4\mathrm{i}C}, \tag{20}$$

where $C = \bar{K}_1 - \bar{\mu}(\frac{x_1}{S_0} - M)$.

The exact solution of the aeroacoustic transfer function for the scattered pressure can be obtained as

$$\mathcal{L}_s(\vec{x}, \omega) = -\frac{\mathrm{e}^{2\mathrm{i}C}}{\mathrm{i}C}\left((1+\mathrm{i})\mathrm{e}^{-2\mathrm{i}C}\sqrt{\frac{B}{B-C}}E^*[2(B-C)] - (1+\mathrm{i})E^*[2B] + 1 - \mathrm{e}^{-2\mathrm{i}C}\right), \tag{21}$$

where $B = \bar{K}_1 + M\bar{\mu} + \bar{\kappa}$ with $\bar{K}_1 = \alpha\bar{K}$.

2. *Far-field acoustic spectrum*

The computation of the far-field acoustic spectrum radiated by the sound source is accomplished through the cross spectrum of Curle's acoustic analogy [1], which relates it to the surface pressure fields. The far-field spectrum at the observer location is expressed as follows:

$$S_{pp}(\vec{x}, \omega) = 4\left(\frac{KMx_3b}{2\pi S_0^2}\right)^2 \frac{S}{2}|\mathcal{L}_o + \mathcal{L}_s|^2 l_y(\omega, k_y) S_{qq}(\omega), \tag{22}$$

where S stands for the airfoil span and S_{qq} is the wall pressure spectrum near the trailing edge, approximately 99% of the chord length as suggested by Lee and Shum [13]. The parameter l_y is the spanwise correlation length near the trailing edge, which is calculated by Corcos' model [51] as follows:

$$l_y(\omega, k_y) = \frac{\omega/(b_c U_c)}{k_y^2 + \omega^2/(b_c U_c)^2}, \tag{23}$$

where $b_c = 1.0$ in this paper. It is worth noting that Eq. (22) yields a magnitude that is four times that of Amiet's original model [6]. This is because the scattering taking place on one side of an airfoil affects both sides [16]. However, it is important to recognize that the incident field should not be influenced by the trailing-edge boundary condition or the Kutta condition. To address this, Li and Lee [52] introduced a correction to Eq. (20), dividing it by a factor of 4. In our analysis, we utilize this modified equation.

III. RESULTS AND DISCUSSION

A. Flow and acoustic fields in LES

The near-field flow and acoustic perturbation at a chord-based Reynolds number of 400 000 and a Mach number of 0.058 at zero angle of attack are first presented. Figure 3 presents an

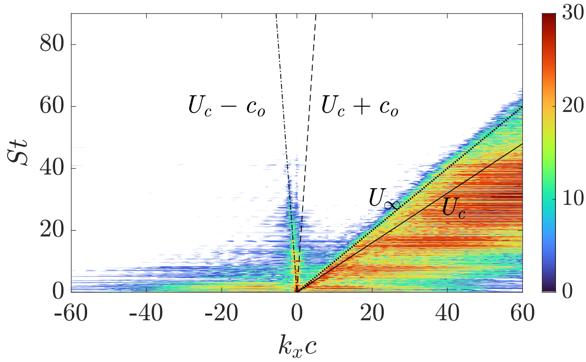

FIG. 4. Spanwise-averaged wave-number-frequency spectrum on the upper side of the airfoil from the leading edge to the trailing edge.

isosurface representation of the Q-criterion [53], with the dilatation field surrounding the airfoil as a background. The Q-criterion, which is normalized using the airfoil chord and inflow freestream speed ($Qc^2/U_\infty^2 = 10$), is equal to a value of 10. In this figure, fully turbulent flows have developed following the breakdown of spanwise-coherent flow structures [54] during the boundary-layer transition process near the leading edge. In the dilatation field, as illustrated in Fig. 3(b), high-frequency wavefronts emanate from the origin of the tripping, a phenomenon commonly observed in squared trip configurations [55]. Notably, strong sound emanating from the trailing edge serves as compelling evidence of trailing-edge noise generation for the simulated case. Despite the spanwise flow perturbations in the boundary-layer tripping region, the convecting turbulent flows for different tripping geometries were not found to influence the spectral characteristics in the vicinity of the trailing edge [56]. The numerical validations concerning time-averaged flows and sound pressure level can be found in the Appendix A.

B. Behaviors of hydrodynamic and acoustic pressures on the wall

In this section, we investigate the wall pressure data derived from LES results. Our objective is to decompose this wall pressure into its hydrodynamic and acoustic components. This decomposition process is achieved through wave-number-frequency decomposition, as detailed in Sec. II D. We place special emphasis on understanding the characteristics and nature of each of these decomposed pressure components acting on the wall.

Figure 4 provides an illustration of the spanwise-averaged wave-number-frequency spectrum on the upper side of the airfoil. In the plot, a wide-band ridge is prominently visible aligned with the freestream velocity U_∞. It is noted that the hydrodynamic pressure is characterized by turbulent convection, displaying high-energy spectra within the convective speed range of U_c. Another noteworthy observation emerges from the spectra along the boundaries of two sound speeds: upstream $U_c - c_o$ and downstream $U_c + c_o$. The upstream acoustic pressure is likely associated with the trailing-edge scattering of coherent structures. In contrast, the downstream acoustic pressure could be attributed to the influence of vortex shedding from trailing-edge bluntness and leading-edge noise sources due to boundary-layer tripping. These aspects will be further explored in subsequent analyses.

Figure 5 presents space-time contour maps for three decomposed pressures in addition to the original pressure. The timescale is normalized using the phase speed of each decomposed pressure to emphasize the propagation effect. The time duration for the original and hydrodynamic pressures spans 1 airfoil FTT, while the duration for the acoustic pressure is 0.1 FTT. As depicted in the plot, the hydrodynamic pressure closely resembles the original pressure, indicating that near-wall pressure fluctuations are primarily governed by streamwise-oriented high-energy and intermittent

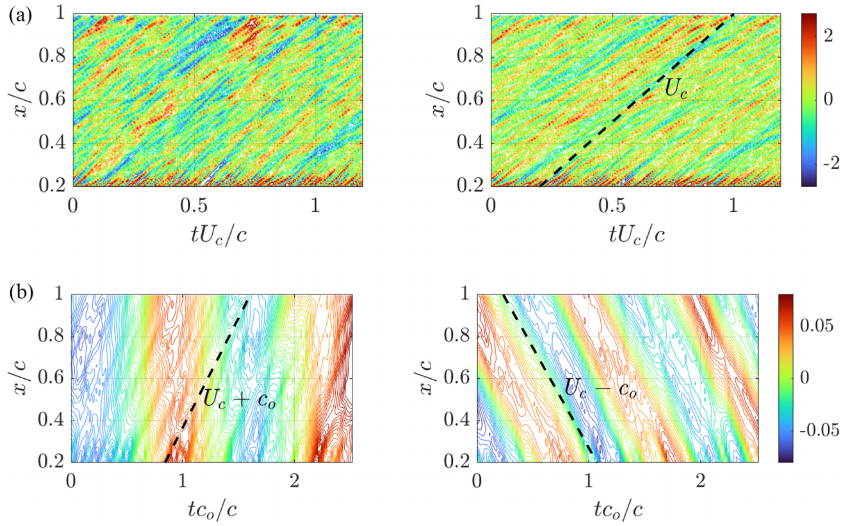

FIG. 5. Space-time map of original and decomposed pressures (Pa): (a) original pressure (left) and hydrodynamic pressure (right), and (b) acoustic pressure in the downstream direction (left) and acoustic pressure in the upstream direction (right). The timescale on the x-axis for the original and hydrodynamic pressures is normalized by the convective velocity, whereas the timescale for the upstream and downstream acoustic pressures is normalized by the speed of sound, c_o. The lines of phase velocity are shown on each decomposed pressure.

turbulent structures, as observed in Refs. [57,58]. The plot effectively captures the intense pressure fluctuations in the flow tripped after $x/c \approx 0.2$ and their time-accurate convection. In Fig. 5(b), the presence of wrinkles represented by contour lines signifies downstream acoustic propagation from the leading edge to the trailing edge. The slight misalignment of the pressure band from the downstream acoustic phase velocity might be likely due to the influence of a long wavelength ($k_x \approx 0$) at a low Strouhal range, $0 < \mathrm{St} < 10$, in the Fourier filtering. The phase speed in this wave-number-frequency domain can mathematically be much greater than the speed of sound, but it physically presents the group of acoustic pressure. On the other hand, the upstream propagation aligns well with its phase speed. Overall, the wave-number-frequency decomposition along the airfoil chord effectively separates the acoustic components from the hydrodynamic pressure disturbances. This representation provides valuable insights into the spatiotemporal dynamics of flow and acoustic components.

Given that both upstream and downstream acoustic pressures exhibit similar phase speeds, these two components are combined into a single acoustic pressure for a comprehensive examination of their source and propagation characteristics in comparison to the hydrodynamic component. Figure 6 illustrates the spanwise-averaged temporal fluctuations for the original, hydrodynamic,

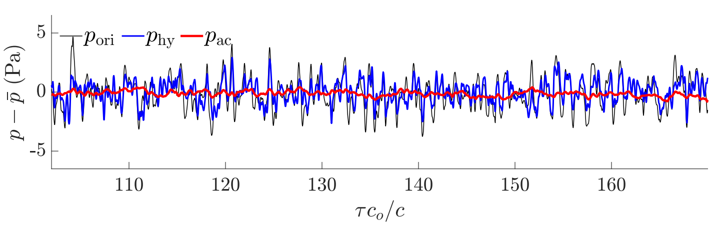

FIG. 6. Spanwise-averaged decomposed wall pressure fluctuations at $x/c \approx 0.99$.

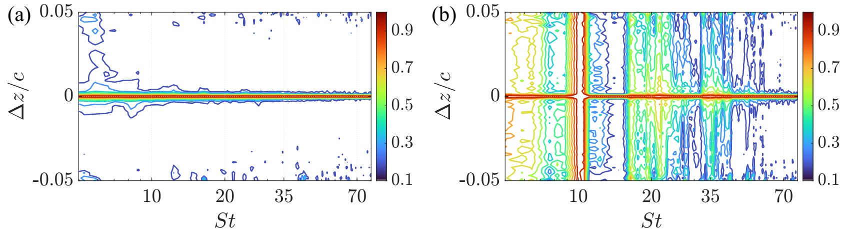

FIG. 7. Contours of spanwise coherence, γ_{pp}^2, at $x/c = 0.99$: (a) hydrodynamic pressure and (b) acoustic pressure.

and acoustic pressures, measured at a reference point located at $x/c = 0.99$ from the leading edge. It is worth noting that the magnitude of the hydrodynamic pressure closely resembles that of the original pressure, while the acoustic pressure exhibits weaker fluctuations. This observation aligns with the common understanding that acoustic energy is a by-product of noise-producing flow fluctuations [59,60]. These findings from the wall will be further cross-examined with the decomposed far-field pressure perturbations in the subsequent section.

The fundamental characteristics of the decomposed wall pressures are statistically evaluated by calculating their coherence and phase relationships. To begin, a spanwise pressure coherence [61,62] is defined as follows:

$$\gamma^2(z, \Delta z, f) = \frac{|\phi_{pp}(z, \Delta z, f)|^2}{|\phi_{pp}(z, 0, f)||\phi_{pp}(z + \Delta z, 0, f)|}, \tag{24}$$

where the cross power spectrum density (CPSD) ϕ_{pp} is the Fourier transform of the space-time cross-correlation function:

$$\phi_{pp}(z, \Delta z, f) = \int_{-\infty}^{\infty} \langle p(z, t)p(z + \Delta z, t + \tau)\rangle \mathrm{e}^{-\mathrm{i}f\tau}\,\mathrm{d}\tau, \tag{25}$$

where $\mathrm{i} = \sqrt{-1}$, and the operator $\langle\cdot\rangle$ denotes the ensemble average over the spanwise separation distance, Δz. In spectral calculations, the Hanning window function is applied before pressure signals are Fourier-transformed.

Figure 7 presents the variation of coherence with respect to the nondimensional separation distance $\Delta z/c$ and the Strouhal number for both the hydrodynamic and acoustic pressures. The coherence pattern of the original pressure, which closely mirrors that of the hydrodynamic pressure, has been omitted from the plot for conciseness. An evident observation is the incoherent nature of the hydrodynamic pressure, whereas the acoustic pressure exhibits strong coherence along the spanwise direction. This observation confirms that the spanwise coherent structure of acoustic pressure disturbances is associated with trailing-edge noise [30,31]. Notably, the spanwise coherence is particularly pronounced at low frequencies around $\mathrm{St} \approx 10$, which can be attributed to the source of vortex shedding noise due to trailing-edge bluntness.

Next, the streamwise pressure coherence is computed based on the spanwise-averaged wall pressure. The original pressure, denoted as p_{ref} and located at $x/c = 0.99$, is used as the reference pressure to assess the coherence between the pressure near the trailing edge and pressures at other locations along the airfoil side. Figure 8 illustrates the streamwise coherence distribution along the upper side of the airfoil for all Strouhal numbers. It is worth noting that the hydrodynamic pressure exhibits only a small region of coherence near the trailing edge, corresponding to the size of coherent turbulent eddies. As one moves further away from the trailing edge, the coherence rapidly diminishes, resulting in an incoherent pattern. In contrast, the acoustic pressure displays significant coherence spanning the entire chord length, particularly in the Strouhal number range of 15–30. At Strouhal numbers less than 10, the straight, uniform coherence lines indicate a compact noise source with a wavelength longer than the acoustic chord length. As the Strouhal numbers increase, the

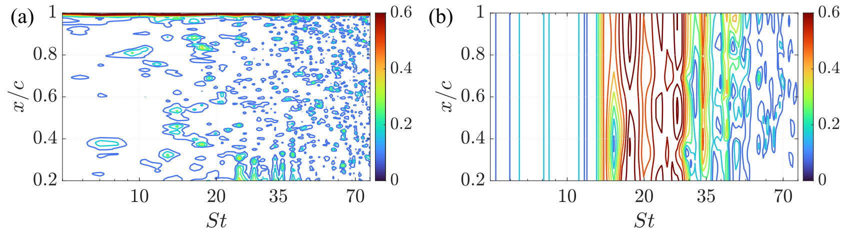

FIG. 8. Contours of streamwise coherence, $\gamma^2_{pp_{\mathrm{ref}}}$. The reference pressure is the original pressure located at $x/c \approx 0.99$: (a) hydrodynamic pressure and (b) acoustic pressure.

appearance of wavy lines signifies noncompact noise sources associated with acoustic scattering. It is important to note that this coherence measure does not account for spectral magnitude but offers valuable insights into the correlation between the point source at the trailing edge and pressure disturbances in other regions.

To gain insights into sound propagation characteristics, including constructive and destructive wave interferences, the phase of the acoustic pressure along the streamwise direction is analyzed. The phase difference between two points is computed as $\mathrm{Re}(\exp(i\phi_{xy}))$, where ϕ_{xy} represents the phase of the CPSD. The subscript x refers to an arbitrary point on the upper side of the airfoil, while the subscript y denotes the fixed reference point at $x/c \approx 0.99$, as used for streamwise and spanwise coherences. Note that the original pressure is used as the reference pressure at a fixed position. Additionally, to observe this phase interference within the local coherent structure for nonfrozen gust [63], the streamwise correlation length is employed:

$$l_x^*(f) = \int_{\xi_1}^{\xi_2} \gamma(\xi, 0, f)\mathrm{d}\xi, \tag{26}$$

where ξ represents the streamwise separation distance normalized by the chord length, and the integration spans from $0.2c$ to x, where turbulent flows are established. Constructive or destructive wave interferences are only meaningful within this streamwise correlation length for the nonfrozen gust case [63]. In this analysis, we place x at the trailing edge, which means that the correlation length is computed at the trailing edge. Equation (26) is validated by comparing it with the empirical model [64], which is provided in the Appendix B. Figure 9 illustrates the streamwise-phase distribution along the airfoil streamwise direction on the upper side. A black dashed line indicates the streamwise correlation length, starting from the trailing edge at St $\approx$ 10, 20, and 35. The phase values close to 1 indicate that the two wall-pressure signals are in-phase, while values close to –1 signify an out-of-phase relationship [62]. The hydrodynamic pressure exhibits high oscillations between neighboring sources across a range of Strouhal numbers, suggesting that destructive interference is a characteristic feature of hydrodynamic pressure, likely associated with the streaky structure in the streamwise direction among turbulence structures [30,31], as observed in Fig. 5(a).

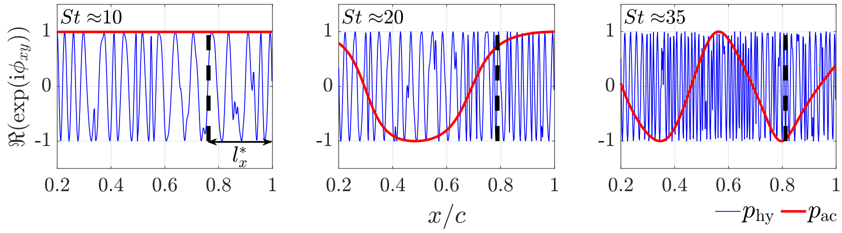

FIG. 9. Spanwise-averaged phase distributions for the hydrodynamic and acoustic pressures along with the streamwise correlation length at the trailing edge at St $\approx$ 10, 20, and 35.

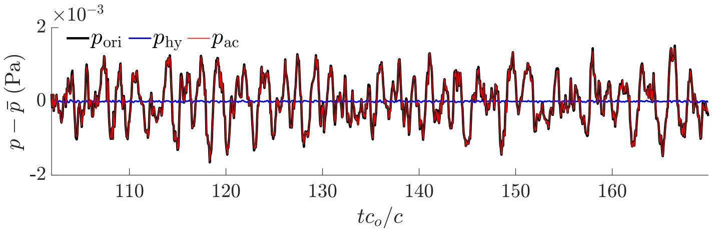

FIG. 10. Radiated pressure fluctuations at an observer location $x/c = 1.0$, $y/c = 10.0$, and $z/c =$ midspan. The far-field pressure is computed from the original or the decomposed pressures on the wall through the FW-H equation.

In contrast, the acoustic pressure shows a much longer waveform. At around St $\approx$ 10, there is a constant in-phase relationship due to the longer wavelength at this frequency, which aligns with the observation of streamwise coherence [Fig. 8(b)]. As the Strouhal number increases, it transitions to a shorter waveform associated with a noncompact source. The waveforms are observed to have one or two periods for the acoustic pressure for the entire airfoil length; however, the phase interference is only effective within the local turbulent coherent structure since the phase interference operates independently at each correlation interval [63]. In this context, the phase alteration for the acoustic pressure within the streamwise correlation length is found to be in phase, making it efficient for sound propagation. These results suggest that the hydrodynamic pressure is ineffective in terms of sound generation due to strong destructive interference, while the acoustic pressure is effective for far-field sound propagation due to constructive interference. This observation will be further supported with more detailed far-field noise analyses and in comparison with analytical models in the subsequent sections.

C. Evaluation of hydrodynamic and acoustic pressures at near and far fields

In this section, the decomposed wall pressures are radiated through the FW-H acoustic analogy to examine the propagating nature of each component at near and far fields. Thus, the far-field pressure fluctuations of each decomposed component are analyzed individually or cross-correlated with near-field pressures to gain deeper insights. Figure 10 plots the contribution from the decomposed wall pressures to the far-field pressure at a receiver, located 10.0c away normal to the origin of the trailing edge in midspan. In contrast to the decomposed wall pressures as shown in Fig. 6, the far-field pressure is significantly affected by the acoustic pressure on the wall, while the hydrodynamic component is negligible. The nonpropagating nature of the hydrodynamic pressure is related to the destructive interference of incoherent turbulent structures in the streamwise direction, as presented in Fig. 9. This characteristic, marked by streamwise oriented turbulent structures [Fig. 5(b)], aligns with the observation that the predominant streaky structures in the turbulent boundary layer have minimal effect on trailing-edge noise [30], whereas the efficiency of sound radiation is more likely related to the spanwise-coherent structure [31,65].

The temporal signals of the propagation from surface hydrodynamic and acoustic pressures, as shown in Fig. 10, are statistically evaluated through the probability density function (PDF). Figure 11 presents PDFs of the original and decomposed pressures. Neither hydrodynamic nor acoustic pressure follows a Gaussian distribution, as indicated by the deviation of one of the tails on the curve from the standard Gaussian shape. This suggests that the original pressure cannot be separated based on the hypothesis that the acoustic pressure follows a Gaussian assumption. This is different from previous observations where the Gaussian assumption was used to separate acoustic pressure from near-field pressure in jet flows at a Mach number of 0.9 using wavelet transform [25]. This observation is consistent with the findings in Ref. [66].

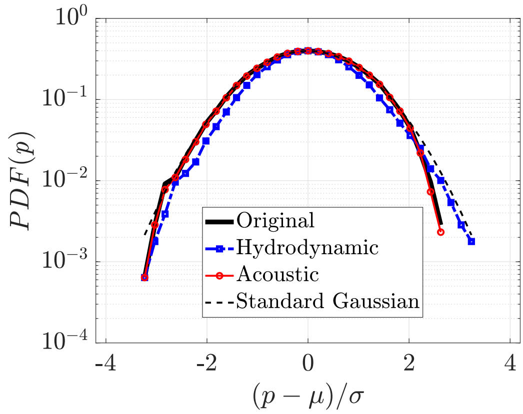

FIG. 11. Polar evolution of PDFs for the far-field pressure that is obtained from the original, hydrodynamic, and acoustic wall pressures with the standard Gaussian distribution at the observer position of $x/c = 1.0$, $x/c = 10.0$, and $z/c =$ midspan.

Visual assessment of sound propagation and dominance near the airfoil for each decomposed pressure is performed by correlating the noise recorded at the far field with the near-field pressure field. The spatial domain pressures are averaged in the spanwise direction. We employ the normalized spatial correlations when the temporal lag is equal to zero, denoted as $R_{\tilde{p}\tilde{p},\tau=0}$, which is a special case of the general definition of cross-correlation [61,67,68] as follows:

$$R_{\tilde{p}\tilde{p}}(\mathbf{x_1}, \mathbf{x_2}, \tau) = \frac{E[\tilde{p}(\mathbf{x_1}, t)\tilde{p}(\mathbf{x_2}, t+\tau)]}{E[\tilde{p}^2(\mathbf{x_1}, t)]^{1/2} E[\tilde{p}^2(\mathbf{x_2}, t)]^{1/2}}, \tag{27}$$

where the operator $\tilde{\cdot}$ stands for the band-pass filter applied to the pressure signal, the operator $E[\cdot]$ denotes the expected value of the signal, and τ is the temporal lag between two signals at point $\mathbf{x_1}$ and point $\mathbf{x_2}$. The threshold for filtering of interest ranged from $9 < \mathrm{St} < 35$, which was found to be the best range from a series of numerical experiments to highlight the physical property of decomposed pressures. The point $\mathbf{x_1}$ is the arbitrary point near the airfoil at which the original pressure is used for the computation of spatial correlation. The reference pressure signal at point $\mathbf{x_2}$ is the far-field pressure propagated from either the hydrodynamic or the acoustic wall pressure measured at the observer location $x/c = 1.0$, $y/c = 10.0$, and $z/c =$ midspan.

Figure 12 provides two contours of filtered normalized spatial correlations: one between the filtered hydrodynamic pressure contribution at the far field and the original pressure in the spatial

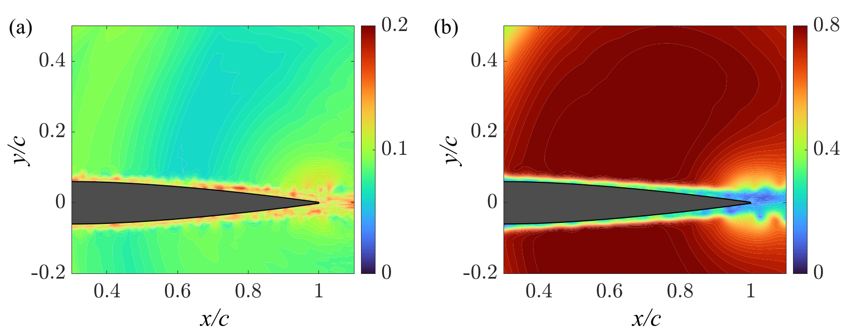

FIG. 12. Normalized spatial correlations R_{pp} filtered at $9 < \mathrm{St} < 35$ overlapped: (a) $R_{\tilde{p}_{\mathrm{ori}}\tilde{p}_{\mathrm{hy,far}},\tau=0}$ and (b) $R_{\tilde{p}_{\mathrm{ori}}\tilde{p}_{\mathrm{ac,far}},\tau=0}$.

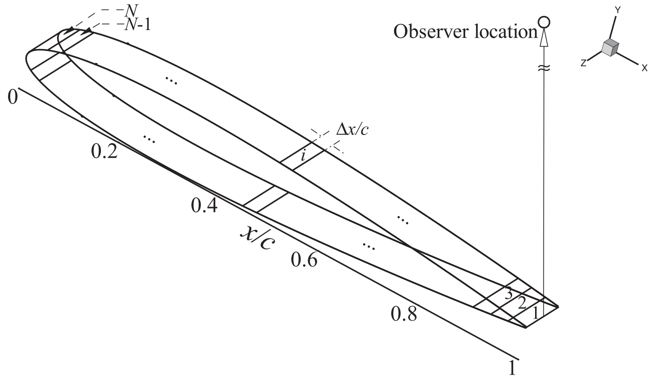

FIG. 13. Schematic of sectional noise analysis. The index starts from the trailing edge. The observer is located at $x/c = 1.0$, $y/c = 10.0$, and $z/c =$ midspan.

domain [Fig. 12(a)], and the other between the filtered acoustic pressure contribution at the far field and the original pressure in the spatial domain [Fig. 12(b)]. The filtered normalized spatial correlations between the far-field hydrodynamic pressure contribution and near-field pressures show a relatively high correlation near boundary-layer flows where turbulent convection is dominant. On the other hand, the filtered normalized spatial correlations between far-field acoustic pressure contribution and near-field pressures are shown to be significantly high away from coherent turbulent flows, indicating the efficient propagation of sound waves.

Our findings revealed that the phase behavior, rather than the source magnitude, has a crucial impact on the differentiation between the roles of hydrodynamic and acoustic pressures, whether they function as actual sound or pseudosound sources. Subsequent analysis entails partitioning the airfoil into strips to emphasize the significance of phase variation. This approach has proven valuable for examining the phase topology of flows around trailing-edge serrations [69] and airfoil-vortex interactions [70]. Figure 13 illustrates the schematic for the sectional noise analysis. The airfoil surface is evenly divided into strips with a width of $\Delta x/c = 0.011$. The wavelength associated with this strip size, corresponding to a Strouhal number on the order of 10^3, is small enough to justify treating the individual strip as a point source. Two different pressures are to be evaluated; one corresponds to the sectional noise radiated from each strip, and the other is derived by gradually accumulating noise from the trailing-edge strip. This allows for a comprehensive analysis of decomposed noises with and without phase effects. All the analyses consider both sides of the airfoil, and the strip starts from the trailing edge, increasing towards the leading edge. Noise radiated by the FW-H acoustic analogy from each strip is measured at the observer positioned $x/c = 1.0$, $y/c = 10.0$, and $z/c =$ midpsan.

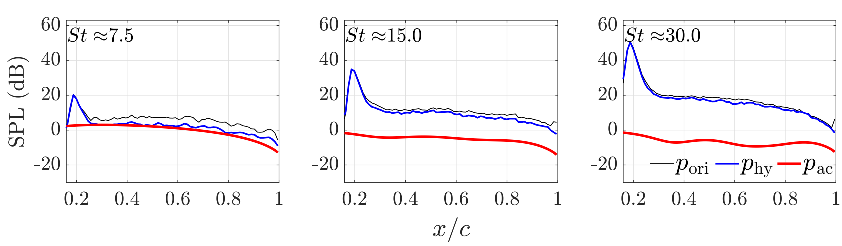

FIG. 14. Octave band SPLs radiated from each strip arranged from the leading-edge region to the trailing edge on both sides of airfoil at St $\approx$ 7.5, 15, and 30.

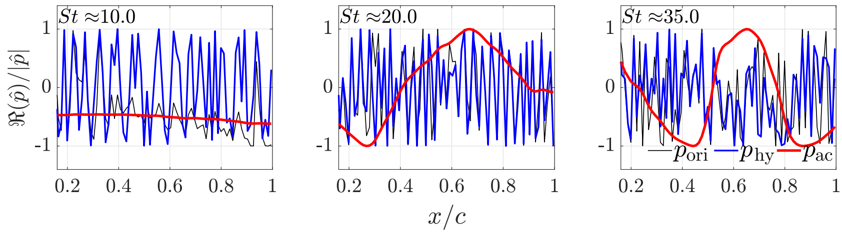

FIG. 15. Phases of airfoil noise radiated from each strip arranged from the leading-edge region to the trailing edge on both sides of airfoil at St ≈ 10, 20, and 35.

Figure 14 displays the octave band SPLs of the original and two decomposed sectional noises emitted from an array of strips on the airfoil surface. In this analysis, the impact of phase interference among neighboring strips is excluded. Remarkably, the influence of the wall-associated hydrodynamic pressure on the far-field acoustics is evident across the entire airfoil, spanning from low to high Strouhal numbers. This effect is attributed to the high turbulent energy levels, which act as a self-noise point source, as indicated in Fig. 12(a). However, the opposite trend applies to the acoustic pressure, with the fluctuations of the acoustic pressure becoming lower than the hydrodynamic component [59,60], which is similar to Fig. 6.

Figure 15 displays the phase distributions of the far-field pressure obtained from the original and decomposed pressures, calculated using the real part of the Fourier-transformed pressure of each strip divided by its absolute value. The phase of the hydrodynamic pressure contribution exhibits a pronounced oscillatory pattern across all Strouhal numbers, mirroring the out-of-phase feature of the coherent structure observed on the wall, as shown in Fig. 9. In contrast, the acoustic pressure contribution demonstrates an in-phase nature akin to what is observed on the wall. This observation highlights that hydrodynamic pressure displays out-of-phase attributes among neighboring turbulent sources, providing crucial evidence that the far-field pressure from the hydrodynamic component is significantly lower than that from the acoustic component.

The cumulative pressure p_i' is calculated by gradually integrating the sectional pressures emitted from each strip as follows:

$$p_i' = \sum_{k=1}^{i} p_k, \tag{28}$$

where p_k stands for the radiated noise from the kth airfoil strip, and the subscript $k = 1$ denotes the trailing-edge strip. This incorporates the phase interference with strips being accumulated. Figure 16 presents a quantitative comparison of the contributions from the two decomposed pressure components against the total pressure for octave band SPLs. In the figure, in-phase and out-of-phase strips primarily represent increases and decreases in the SPL level as the airfoil strip at the trailing

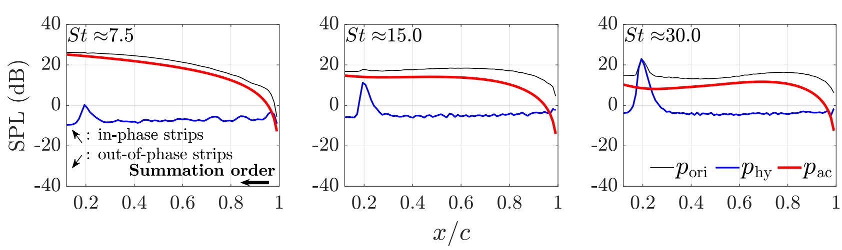

FIG. 16. Cumulative octave band SPLs radiated from each strip arranged from the leading-edge region to the trailing edge on both sides of airfoil at St ≈ 7.5, 15, and 30.

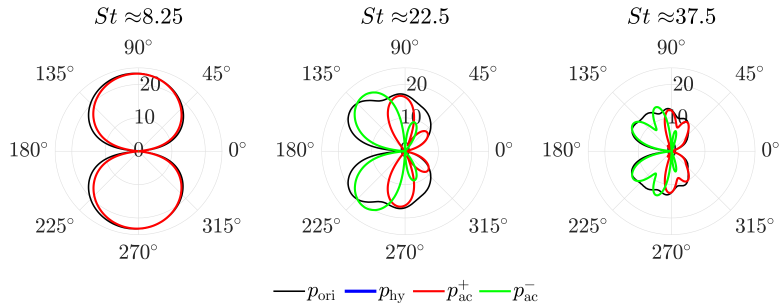

FIG. 17. Directivity of the far-field pressures obtained from the original and decomposed wall pressures at the radius of 10.0c from the trailing-edge origin.

edge is gradually integrated toward the leading edge. This is simply denoted by the upward and downward arrows to clearly indicate the streamwise phase behavior of the SPL curve when integrated. One can observe nearly uniform sound strength with small fluctuations in the cumulative noise originating from hydrodynamic wall pressure. This uniform sound level across the airfoil underscores the typical phenomenon of destructive interference caused by streamwise incoherent turbulent eddies or streamwise turbulent structures [57,58]. There is a sudden increase in sound near the tripping region due to a local perturbation induced by the trip, but this spike is subsequently mitigated as a result of interactions between upward and downward scattering around the trip. Despite this cancellation, leading-edge noise near the tripped region contributes slightly to the total or original sound at higher frequencies.

Conversely, cumulative noise generated by acoustic wall pressure exhibits a progressive increase as strips are integrated. This can be attributed to constructive, in-phase relationships with neighboring sources. This in-phase nature is particularly notable at lower Strouhal numbers, where the corresponding wavelength exceeds the airfoil chord length. Another significant observation is the abrupt increase in noise from the trailing edge to approximately $x/c \approx 0.8$, coinciding with the region where edge scattering has a substantial impact. This region closely aligns with the streamwise correlation length, as illustrated in Fig. 9. The width of approximately $x/c \approx 0.2$ suggests efficient scattering within the streamwise correlation length, which is shorter than the phase period of the acoustic wave for all frequencies considered. Overall, the nonpropagating behavior arises for the hydrodynamics pressure from the out-of-phase relationships between neighboring strips, leading to rapid dissipation as evanescent waves. In contrast, noise radiation is found to be efficient for edge-scattered acoustic pressure due to in-phase behavior.

Figure 17 presents the directivity patterns for the far-field sound spectra obtained from the original and decomposed pressures at three specific Strouhal numbers, highlighting two distinct propagating directions for acoustic pressure. The downstream-traveling acoustic pressure is denoted as p_{ac}^{+}, while the upstream-propagating acoustic pressure is denoted as p_{ac}^{-}. At St $\approx$ 8.25, one can observe that the downstream-traveling acoustic pressure forms a compact dipolar pattern, which corresponds to a shorter acoustic source length or chord length than the wavelength. When the noise source is nearly noncompact, the upstream-propagating pressure dominates, creating a forward cardioid pattern. The rearward lobes spanning below 90° are contributed by the downstream-traveling acoustic pressure. While decomposed pressures p_{ac}^{-} dominated by trailing-edge scattering and p_{ac}^{+} dominated by diffraction from leading-edge tripping installation show distinct lobes at St $\approx$ 37.5, the lobe pattern is alleviated for the total pressure. This results from the interaction of those multiple noise sources, although the strength of p_{ac}^{+} is much smaller than that of p_{ac}^{-} in the upstream direction. In contrast, the magnitude of hydrodynamic pressure is negligible due to destructive interference among coherent turbulent structures. Although the magnitude of hydrodynamic pressure is minimal, its nonlinear interaction with varying wave numbers in the streamwise and spanwise directions

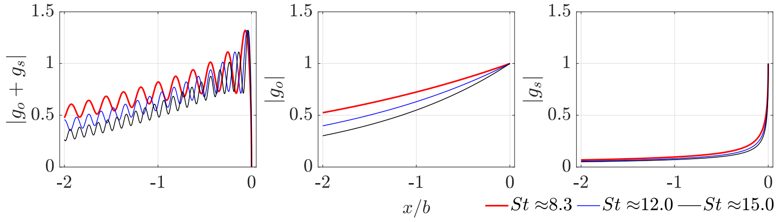

FIG. 18. Magnitude of summation of incident (g_o) and scattered (g_s) wall pressures and each separate component side by side for three Strouhal numbers.

under large-to-small turbulent flows may alter the phase relationship between acoustic and total pressures [71]. These alterations can lead to an imperfect overlap of the total and acoustic pressure directivity patterns and their magnitudes, as similarly observed in Figs. 14 and 16.

D. Incident and scattered pressures in Amiet's trailing-edge noise theory

The previous sections have explored the inherent characteristics of hydrodynamic and acoustic pressures, which were obtained through wave-number-frequency filtering within the numerical framework. In this section, we shift our focus to evaluate the role of incident and scattered pressures on the wall and in the far field in the framework of an analytical solution of Amiet's model. These pressures are derived based on assumptions stemming from flat plate geometry and the frozen turbulence hypothesis [11], as detailed in Sec. II F.

Figure 18 presents the magnitudes of the incident and scattered pressures, as well as their cumulative values, across various Strouhal numbers. These wall pressures are calculated using Eqs. (16) and (17), respectively. The incident pressure exhibits exponential decay at all Strouhal numbers, with the rate of decay controlled by the parameter ϵ in Eq. (16). On the other hand, the scattered pressure reaches its maximum magnitude at the trailing edge and then rapidly decays from the trailing edge to the leading edge. This behavior is consistent with the idea that edge scattering is most significant near the trailing edge. This aligns with the numerical framework in which the increase in acoustic pressure significantly occurs within 20% of the chord length near the trailing edge, as illustrated in Fig. 16, although Amiet's model uses a frozen gust assumption. It is important to note that while the magnitudes of the incident and scattered pressures are equal at the trailing edge, their cumulative value or total pressure is not simply the algebraic sum of the two pressures. Additionally, the combined pressure exhibits a distinct and highly oscillatory pattern, which will be further examined in the subsequent phase analysis.

The phase variation along the airfoil chord is effectively represented by the real part of the wall pressure divided by its own magnitude. Figure 19 plots the phase variation along the chord for the total, incident, and scattered pressures. Notably, the incident pressure exhibits highly oscillatory phases, while the phase of the scattered pressure transitions from monotonic to sinusoidal waves as

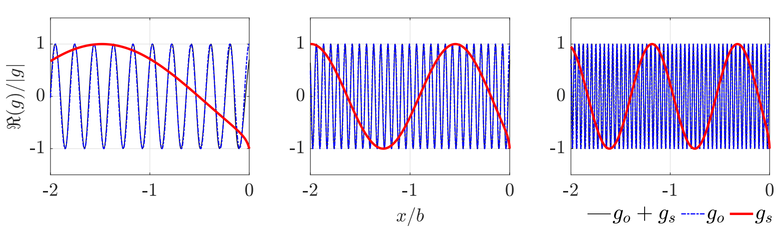

FIG. 19. Phase of summation of incident (g_o) and scattered (g_s) wall pressures and each component side by side. Strouhal numbers are 8.3, 22.5, and 37.5 from left to right.

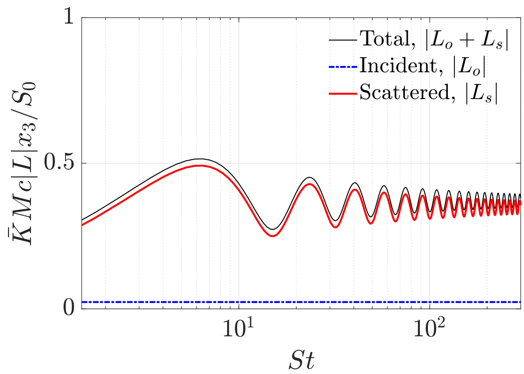

FIG. 20. Normalized aeroacoustic transfer functions of the summation of incident and scattered components along with each separate component at a microphone position of $x/c = 1.0$, $y/c = 10.0$, and $z/c =$ midspan.

the Strouhal number increases. The phase of the total pressure is mainly influenced by the incident pressure, given its higher amplitude than the scattered pressure, as evident in Fig. 18. It should be noted that these phase dynamics observed in the incident and scattered pressures are comparable to those of hydrodynamic and acoustic pressures in numerical simulations, as presented in Figs. 9 and 15, although pairs of pressures are derived from different principles of decomposition.

Figure 20 illustrates the normalized incident, scattered, and total aeroacoustic transfer functions, which play a crucial role in calculating the radiated sound spectra in accordance with Amiet's theory [Eq. (22)]. These are obtained through the integration of the wall pressures using the analytical formulations provided in Eqs. (20) and (21), respectively. The scattered pressure is found to exhibit higher magnitudes than the incident pressure across the entire frequency range. This contrasts with the observation in Fig. 18, where the overall magnitude of the incident wall pressure surpasses that of the scattered pressure, except at the trailing edge. However, this is a consistent observation with Fig. 10, where the acoustic pressure significantly contributes to the total pressure. The nonpropagating physics of incident pressure is a direct result of the destructive interference, as evidenced by the highly oscillatory pattern depicted in Fig. 19.

Figure 21 provides the directivity patterns of incident, scattered, and total pressures across a range of Strouhal numbers. A dominant compact dipole pattern is evident at St $\approx$ 8.25, resulting in significant noise in all directions. The multilobed pattern emerges at higher Strouhal numbers, primarily derived from the scattered pressure. This aligns with the typical directional characteristics of trailing-edge noise [72,73]. The consistent dominance of scattered pressure across the entire

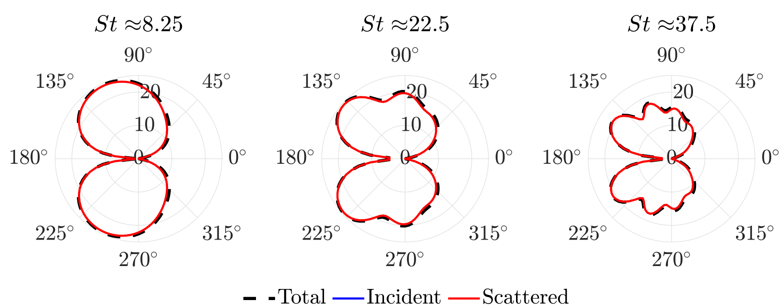

FIG. 21. Directivity of the one-third octave band SPLs for the summation of the incident and scattered parts and each separate component at the radius of 10.0c from the trailing-edge origin.

range of Strouhal numbers, particularly in contributing to the total pressure associated with the cardioid directivity pattern observed between Strouhal numbers 22.5 and 37.5, further reinforces its role as the primary source of far-field acoustic pressure, as established in the preceding numerical analysis. It is noteworthy that our findings differ from those of Martínez-Lera *et al.* [21], where the hydrodynamic pressure was reported to dominate at low frequencies. Furthermore, Amiet's theory indicates that the magnitudes and directional patterns of scattered and total pressures exhibit greater similarity compared to those of total and acoustic pressures observed in the numerical approach. One potential explanation is that Amiet's theory was developed under assumptions involving frozen turbulence [11] and infinitely long spans with a flat plate configuration. Consequently, the role of the incident pressure might have a lesser influence on the interaction between total and scattered pressures, resulting in similar magnitude levels between the two pressures. This aligns with the indirect demonstration by Tiomkin and Jaworski [71], where the relaxation of frozen turbulence gust by a linearly varying wave number significantly alters the total acoustics due to its impact on the incident pressure. Overall, a key insight derived from Amiet's analytical approach, in relation to the numerical analysis, is that the scattered or acoustic pressure exhibits an in-phase characteristic, which significantly contributes to the far-field sound. On the other hand, the incident or hydrodynamic pressure demonstrates a pseudosound nature due to destructive interference with the oscillatory phase along the chord, even though the magnitude of wall pressure is higher than that of the scattered or acoustic pressure.

IV. CONCLUSIONS

In this study, we conducted an in-depth examination of the fundamental characteristics of hydrodynamic (incident) and acoustic (scattered) pressures, providing insights into the complexities of sound propagation within turbulent boundary-layer flows, with a specific emphasis on trailing-edge noise. We carried out a detailed analysis of pressure fields surrounding a NACA 0012 airfoil, which was tripped near the leading edge. This analysis was performed using high-fidelity LES at zero incidence angle. The hydrodynamic and acoustic pressures were decomposed through wavenumber-frequency filtering within the numerical framework. Additionally, we analyzed incident and scattered pressures based on Amiet's analytical formulations. Subsequently, we related these decomposed wall pressures to the far field using both the FW-H equation and Amiet's theory.

This paper uncovered distinctive characteristics of hydrodynamic pressure. This pressure source arises from streamwise-oriented turbulent structures along the wall, with phase velocities close to the convective speed, U_c. These turbulent structures exhibit incoherence between adjacent turbulent eddies, resulting in highly oscillatory phase variations, which give rise to nonpropagating or evanescent waves. Consequently, the far-field noise radiated from the hydrodynamic pressure remained significantly lower than that of the decomposed acoustic component. Despite acting as an inherently pseudosound source by itself, the hydrodynamic pressure played a crucial role in generating acoustic pressure, driven by spanwise-coherent turbulent structures near the trailing edge.

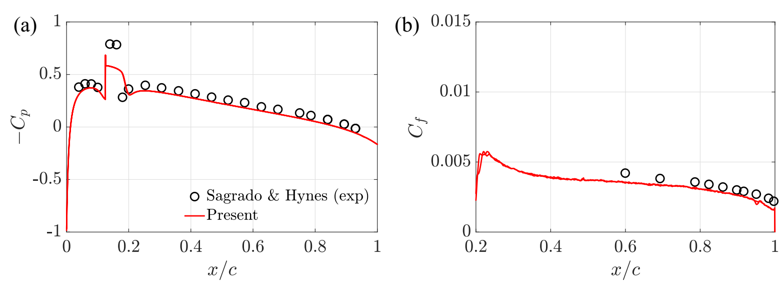

FIG. 22. Time-averaged flow characteristics: (a) the surface pressure coefficient and (b) the friction coefficient on the airfoil against the tripped experiment [74].

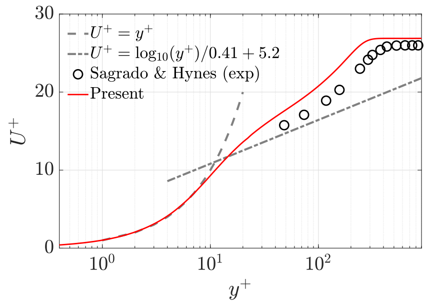

FIG. 23. Time-averaged velocity profile normalized by friction velocity along the wall units against the tripped experiment [74] at $x/c = 0.88$.

Furthermore, the presence of hydrodynamic pressure was identified as a contributing factor to the differences in magnitude and directional characteristics between total and acoustic pressures. Our study also demonstrated that the physical properties of incident pressure in the analytical approach align with those derived from the decomposed hydrodynamic pressure on the wall and at the far field.

The acoustic pressure exhibited efficient propagation to the far field. Despite the significantly lower magnitude of the acoustic pressure source on the wall than that of the hydrodynamic pressure, it played a predominant role in shaping far-field sound spectra. This predominance was attributed to the in-phase behavior of the acoustic pressure, which was particularly pronounced in the case of compact dipolar sources at lower Strouhal numbers. Even at higher Strouhal numbers, the in-phase tendencies persisted within the streamwise correlation length, facilitating efficient sound propagation across the entire frequency range. It is worth noting that noncompact noise sources or the streamwise correlation length near the trailing edge covered approximately 20% of the trailing edge. These areas were identified as regions of proficient trailing-edge scattering.

This research, which elucidates the distinct roles of hydrodynamic incident pressure and acoustic scattered pressure, is expected to significantly enhance our understanding of scattering phenomena associated with broadband trailing-edge noise in wall-bounded flows. Furthermore, it provides valuable insights into ongoing discussions about the fundamental mechanisms influencing noise reduction when airfoil serrations are applied near the trailing edge, offering guidance on which specific noise sources should be targeted for reduction.

APPENDIX A: VALIDATION OF COMPUTATIONAL CASES

The validation process involves comparing the pressure, skin friction coefficients, and boundary-layer velocity profile with experimental data [74] under specific conditions, including a chord-based Reynolds number of 400 000 and a Mach number of 0.058. Additionally, the far-field acoustic spectra are validated against measurements of SPL by Brooks *et al.* [3] at a chord-based Reynolds number of 320 000 and a Mach number of 0.093. In both cases, a zero incidence angle is considered. Figure 22 presents the time-averaged negative pressure coefficient $-C_p$ and the friction coefficient C_f, which are compared side by side with the experimental results obtained by Garcia-Sagrado and Hynes [74]. Notably, the predicted pressure curve exhibits a sharp suction peak, reflecting the enforced transition by tripping and closely approximating the experimental data. Both aerodynamic quantities, $-C_p$ and C_f, show good agreement with the experimental measurements. Figure 23 shows the time-averaged boundary-layer velocity profile at $x/c = 0.88$. Good agreement is observed in the inner layer and up to $y^+ \approx 50$ within the logarithmic layer when compared with the law of the wall, where the high coherence between wall pressure and velocity profile is particularly significant [66]. While the velocity profile exhibits a similar shape, a slight deviation beyond $y^+ \approx 50$ may be attributed to differences in the tripping approach.

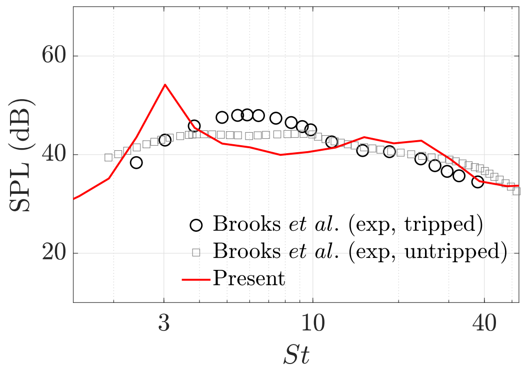

FIG. 24. Sound pressure level at an observer location $x/c = 1.0$, $y/c = 8.0$, $z/c =$ midspan compared with tripped and untripped experiments [3].

Figure 24 illustrates the predicted one-third octave band SPL, compared to the untripped and tripped experimental measurements. The sound receiver is located at a position $8.0c$ normal to the origin of the trailing edge at midspan. In the experiment by Brooks *et al.* [3], the trip was introduced by the random distribution of grit in strips, which is different from the spanwise extrusion of the squared trip dot used in the current simulation. Both the numerical and experimental cases position the trip at $x/c \approx 0.2$. Since the spanwise length of the numerical model is 20 times shorter than the wind tunnel setup, a correction proposed by Kato *et al.* [75] has been applied to the one-third octave SPL obtained numerically. One notable observation is the presence of a tonal peak around $\mathrm{St} = 3$ in the prediction, while this feature is absent in both experiments. This tonal noise originates from vortex shedding induced by the blunt trailing edge, with $h_{\mathrm{TE}}/\delta^* \approx 0.5$, whereas the experiment employs a sharp edge. The choice of a blunt trailing edge in the simulation is motivated by its ability to produce better mesh quality near the trailing edge. The origin of the low-frequency tonal peak was identified near the trailing edge through dynamic mode decomposition [66]. Sound spectra at frequencies less than $\mathrm{St} = 10$ are slightly underpredicted, which is lower than the untripped experimental case. This may be attributed to the retardation of the laminar-to-turbulent transition, as depicted in Fig. 3. This difference in the laminar-to-turbulent transition is likely due to the two-dimensional characteristics of tripping in the simulation, which might be absent in the experimental setup. Beyond a high-frequency broadband range exceeding $\mathrm{St} = 10$, the prediction shows a weak small hump due to boundary-layer tripping but overall demonstrates good agreement with the tripped experimental data.

APPENDIX B: VALIDATION OF THE STREAMWISE CORRELATION LENGTH

Figure 25 presents a comparison of the streamwise correlation lengths derived from Eq. (26) and those predicted by the Smol'yakov model. The Smol'yakov model [64] is formulated as follows:

$$l_x(\omega) = \frac{U_c}{\alpha_x \omega} A^{-1}, \tag{B1}$$

with

$$A = \left[1 - \frac{\beta U_c}{\omega \delta^*} + \left(\frac{\beta U_c}{\omega \delta^*}\right)^2\right]^{1/2}. \tag{B2}$$

Here, $\alpha_x = 0.124$ and $\beta = 0.25$. The convection velocity is defined as

$$\frac{U_c(\omega)}{U_0} = \frac{1.6\omega\delta^*/U_0}{1 + 16(\omega\delta^*/U_0)^2} + 0.6. \tag{B3}$$

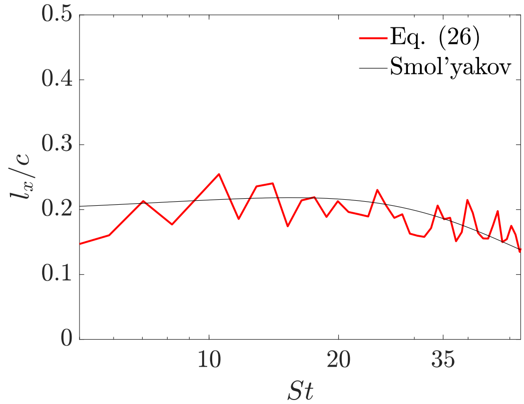

FIG. 25. Streamwise correlation lengths for Eq. (26) and the Smol'yakov model.

The displacement thickness, δ^*, is calculated from the LES at $x/c = 0.996$. The agreement between these two models shown in Fig. 25 validates the current numerical approach for calculating the correlation length under nonhomogeneous turbulent flows over the finite chord.

[1] N. Curle, The influence of solid boundaries upon aerodynamic sound, Proc. R. Soc. London, Ser. A **231**, 505 (1955).

[2] M. Wang, J. Freund, and S. Lele, Computational prediction of flow-generated sound, Annu. Rev. Fluid Mech. **38**, 483 (2006).

[3] T. F. Brooks, D. S. Pope, and M. A. Marcolini, *Airfoil Self-Noise and Prediction*, Tech. Rep. NASA-RP-1218 (National Aeronautics and Space Administration, 1989).

[4] S. Lee, L. Ayton, F. Bertagnolio, S. Moreau, T. Chong, and P. Joseph, Turbulent boundary layer trailing-edge noise: Theory, computation, experiment, and application, Prog. Aerosp. Sci. **126**, 100737 (2021).

[5] J. E. Ffowcs Williams and L. Hall, Aerodynamic sound generation by turbulent flow in the vicinity of a scattering half plane, J. Fluid Mech. **40**, 657 (1970).

[6] R. K. Amiet, Acoustic radiation from an airfoil in a turbulent stream, J. Sound Vib. **41**, 407 (1975).

[7] R. K. Amiet, Noise due to turbulent flow past a trailing edge, J. Sound Vib. **47**, 387 (1976).

[8] R. K. Amiet, Effect of the incident surface pressure field on noise due to turbulent flow past a trailing edge, J. Sound Vib. **57**, 305 (1978).

[9] M. S. Howe, A review of the theory of trailing-edge noise, J. Sound Vib. **61**, 437 (1978).

[10] M. Lighthill, On sound generated aerodynamically I. General theory, Proc. R. Soc. A: Math. Phys. Eng. Sci. **211**, 564 (1952).

[11] G. Taylor, The spectrum of turbulence, Proc. R. Soc. London **164**, 476 (1938).

[12] S. Lee, Empirical wall-pressure spectral modeling for zero and adverse pressure gradient flows, AIAA J. **56**, 1818 (2018).

[13] S. Lee and J. Shum, Prediction of airfoil trailing edge noise using empirical wall pressure spectrum models, AIAA J. **57**, 888 (2019).

[14] S. Li and S. Lee, Prediction of rotorcraft broadband trailing-edge noise and parameter sensitivity study, J. Am. Helicopter Soc. **65**, 1 (2020).

[15] S. Li and S. Lee, Prediction of urban air mobility multirotor VTOL broadband noise using UCD-QuietFly, J. Am. Helicopter Soc. **66**, 1 (2021).

[16] M. Roger and S. Moreau, Back-scattering correction and further extensions of Amiet's trailing-edge noise model. Part I: Theory, J. Sound Vib. **286**, 477 (2005).

[17] S. Moreau, M. Roger, and V. Jurdic, Effect of angle of attack and airfoil shape on turbulence-interaction noise, in *Proceedings of the 11th AIAA/CEAS Aeroacoustics Conference* (AIAA, Reston, VA, 2005), AIAA paper 2005–2973.

[18] A. Oberai, F. Roknaldin, and T. Hughes, Computation of trailing-edge noise due to turbulent flow over an airfoil, AIAA J. **40**, 2206 (2002).

[19] Y. Khalighi, A. Mani, F. Ham, and P. Moin, Prediction of sound generated by complex flows at low Mach numbers, AIAA J. **48**, 306 (2010).

[20] P. Martínez-Lera, C. Schram, H. Bériot, and R. Hallez, An approach to aerodynamic sound prediction based on incompressible-flow pressure, J. Sound Vib. **333**, 132 (2014).

[21] P. Martínez-Lera, J. Christophe, and C. Schram, Computation of the self-noise of a controlled-diffusion airfoil based on the acoustic analogy, Int. J. Aeroacoust. **16**, 44 (2017).

[22] M. Terracol, E. Manoha, C. Herrero, E. Labourasse, S. Redonnet, and P. Sagaut, Hybrid methods for airframe noise numerical prediction, Theor. Comput. Fluid Dyn. **19**, 197 (2005).

[23] C. Tinney and P. Jordan, The near pressure field of co-axial subsonic jets, J. Fluid Mech. **611**, 175 (2008).

[24] S. Grizzi and R. Camussi, Wavelet analysis of near-field pressure fluctuations generated by a subsonic jet, J. Fluid Mech. **698**, 93 (2012).

[25] M. Mancinelli, T. Pagliaroli, A. Di Marco, R. Camussi, and T. Castelain, Wavelet decomposition of hydrodynamic and acoustic pressures in the near field of the jet, J. Fluid Mech. **813**, 716 (2017).

[26] S. Shubham, R. Sandberg, S. Moreau, and H. Wu, Surface pressure spectrum variation with Mach number on a CD airfoil, J. Sound Vib. **526**, 116762 (2022).

[27] P. Schmid, Dynamic mode decomposition of numerical and experimental data, J. Fluid Mech. **656**, 5 (2010).

[28] Y. Kojima, C. S. Skene, C. A. Yeh, K. Taira, and M. Kameda, On the origin of quadrupole sound from a two-dimensional airfoil trailing edge, J. Fluid Mech. **958**, A3 (2023).

[29] M. Sanjose, A. Towne, P. Jaiswal, S. Moreau, S. Lele, and A. Mann, Modal analysis of the laminar boundary layer instability and tonal noise of an airfoil at Reynolds number 150,000, Int. J. Aeroacoust. **18**, 317 (2019).

[30] A. Sano, L. I. Abreu, A. V. G. Cavalieri, and W. R. Wolf, Trailing-edge noise from the scattering of spanwise-coherent structures, Phys. Rev. Fluids **4**, 094602 (2019).

[31] L. Abreu, A. Tanarro, A. Cavalieri, P. Schlatter, R. Vinuesa, A. Hanifi, and D. Henningson, Spanwise-coherent hydrodynamic waves around flat plates and airfoils, J. Fluid Mech. **927**, A1 (2021).

[32] A. Towne, O. Schmidt, and T. Colonius, Spectral proper orthogonal decomposition and its relationship to dynamic mode decomposition and resolvent analysis, J. Fluid Mech. **847**, 821 (2018).

[33] D. Kang and S. Lee, Cross-spectrum method for acoustic source identification and visualization of airfoil noise, Aerosp. Sci. Technol. **151**, 109278 (2024).

[34] J. E. Ffowcs Williams and D. Hawkings, Sound generation by turbulence and surfaces in arbitrary motion, Philos. Trans. Math. Phys. Eng. Sci. **264**, 321 (1969).

[35] J. M. Turner and J. W. Kim, Effect of spanwise domain size on direct numerical simulations of airfoil noise during flow separation and stall, Phys. Fluids **32**, 065103 (2020).

[36] J. M. Turner and J. W. Kim, Aerofoil dipole noise due to flow separation and stall at a low Reynolds number, Int. J. Heat Fluid Flow **86**, 108715 (2020).

[37] D. Kang and S. Lee, Aerodynamic and aeroacoustic effects of different transition mechanisms on an airfoil, AIAA J. **62**, 1517 (2024).

[38] N. J. Georgiadis, D. P. Rizzetta, and C. Fureby, Large-Eddy simulation: Current capabilities, recommended practices, and future research, AIAA J. **48**, 1772 (2010).

[39] P. Moin, K. Squires, W. Cabot, and S. Lee, A dynamic subgrid-scale model for compressible turbulence and scalar transport, Phys. Fluids **3**, 2746 (1991).

[40] U. Piomelli, Large-eddy simulation: Present state and future perspectives, in *Proceedings of the 36th AIAA Aerospace Sciences Meeting and Exhibit* (AIAA, Reston, VA, 1998), AIAA paper 1998–534.

[41] J. Blazek, *Computational Fluid Dynamics: Principles and Applications* (Butterworth-Heinemann, Kidlington, Oxford, UK, 2015).

[42] A. Favre, Equations des gaz turbulents compressibles, J. Mec. **4** (1965).

[43] F. Nicoud and F. Ducros, Subgrid-scale stress modelling based on the square of the velocity gradient tensor, Flow Turbul. Combust. **62**, 183 (1999).

[44] H. Weller, G. Tabor, H. Jasak, and C. Fureby, A tensorial approach to computational continuum mechanics using object-oriented techniques, Comput. Phys. **12**, 620 (1998).

[45] F. Menter, Two-equation eddy-viscosity turbulence models for engineering applications, AIAA J. **32**, 1598 (1994).

[46] K. S. Brentner and F. Farassat, Modelling aerodynamically generated sound of helicopter rotors, Prog. Aerosp. Sci. **39**, 83 (2003).

[47] G. A. Brès, K. S. Brentner, G. Perez, and H. E. Jones, Maneuvering rotorcraft noise prediction, J. Sound Vib. **275**, 719 (2004).

[48] S. Lee, K. Brentner, F. Farassat, and P. Morris, Analytic formulation and numerical implementation of an acoustic pressure gradient prediction, J. Sound Vib. **319**, 1200 (2009).

[49] R. Schlinker and R. Amiet, Helicopter rotor trailing edge noise, in *Proceedings of the 7th Aeroacoustics Conference* (AIAA, Reston, VA, 1981), AIAA paper 1981–2001.

[50] M. Abramowitz, *Handbook of Mathematical Functions* (Dover Publications, Washington, D.C., 1970).

[51] G. Corcos, The structure of the turbulent pressure field in boundary-layer flows, J. Fluid Mech. **18**, 353 (1964).

[52] S. Li and S. Lee, Analytic prediction of rotor broadband noise with serrated trailing edges, in *Proceedings of the 78th VFS International Annual Forum* (Vertical Flight Society, Fort Worth, TX, 2021).

[53] J. C. R. Hunt, A. A. Wray, and P. Moin, Eddies, streams, and convergence zones in turbulent flows, in *Studying Turbulence Using Numerical Simulation Databases, 2. Proceedings of the 1988 Summer Program* (National Aeronautics and Space Administration, 1998).

[54] F. White and J. Majdalani, *Viscous Fluid Flow* (McGraw-Hill, New York, 2006).

[55] A. Bodling and A. Sharma, Numerical investigation of noise reduction mechanisms in a bio-inspired airfoil, J. Sound Vib. **453**, 314 (2019).

[56] J. Winkler, H. Wu, S. Moreau, T. Carolus, and R. Sandberg, Trailing-edge broadband noise prediction of an airfoil with boundary-layer tripping, J. Sound Vib. **482**, 115450 (2020).

[57] J. Jiménez, Near-wall turbulence, Phys. Fluids **25**, 101302 (2013).

[58] L. Abreu, A. Cavalieri, P. Schlatter, R. Vinuesa, and D. Henningson, Spectral proper orthogonal decomposition and resolvent analysis of near-wall coherent structures in turbulent pipe flows, J. Fluid Mech. **900**, A11 (2020).

[59] M. Wang and P. Moin, Computation of trailing-edge flow and noise using large-eddy simulation, AIAA J. **38**, 2201 (2000).

[60] T. Colonius and S. Lele, Computational aeroacoustics: Progress on nonlinear problems of sound generation, Prog. Aerosp. Sci. **40**, 345 (2004).

[61] K. Shin and J. Hammond, *Fundamentals of Signal Processing for Sound and Vibration Engineers* (Wiley, West Sussex, England, 2008).

[62] J. W. Kim, S. Haeri, and P. F. Joseph, On the reduction of airfoil–turbulence interaction noise associated with wavy leading edges, J. Fluid Mech. **792**, 526 (2016).

[63] H. Tian and B. Lyu, The impact of non-frozen turbulence on the modelling of the noise from serrated trailing edges, J. Fluid Mech. **990**, A4 (2024).

[64] A. Smol'yakov, A new model for the cross spectrum and wavenumber-frequency spectrum of turbulent pressure fluctuations in a boundary layer, Acoust. Phys. **52**, 331 (2006).

[65] P. Nogueira, A. Cavalieri, and P. Jordan, A model problem for sound radiation by an installed jet, J. Sound Vib. **391**, 95 (2017).

[66] D. Kang, S. Lee, D. Brouzet, and S. K. Lele, Wavelet-based pressure decomposition for airfoil noise in low-Mach number flows, Phys. Fluids **35**, 075112 (2023).

[67] C. Bogey and C. Bailly, An analysis of the correlations between the turbulent flow and the sound pressure fields of subsonic jets, J. Fluid Mech. **583**, 71 (2007).

[68] C. Jiang, D. Moreau, C. de Silva, and C. Doolan, Noise generation mechanisms of a micro-tube porous trailing edge, J. Sound Vib. **571**, 118085 (2023).

[69] F. Avallone, W. C. P. Van Der Velden, D. Ragni, and D. Casalino, Noise reduction mechanisms of sawtooth and combed-sawtooth trailing-edge serrations, J. Fluid Mech. **848**, 560 (2018).

[70] J. M. Turner and J. W. Kim, On the universal trends in the noise reduction due to wavy leading edges in aerofoil–vortex interaction, J. Fluid Mech. **871**, 186 (2019).

[71] S. Tiomkin and J. Jaworski, Revisiting the frozen gust assumption through the aeroacoustic scattering of wavepackets by a semi-infinite plate, J. Sound Vib. **571**, 117989 (2023).

[72] G. Desquesnes, M. Terracol, and P. Sagaut, Numerical investigation of the tone noise mechanisms over laminar airfoils, J. Fluid Mech. **591**, 155 (2007).

[73] W. Wolf, J. Azevedo, and S. Lele, Convective effects and the role of quadrupole sources for airfoil aeroacoustics, J. Fluid Mech. **708**, 502 (2012).

[74] A. Garcia-Sagrado and T. Hynes, Wall pressure sources near an airfoil trailing edge under turbulent boundary layers, J. Fluids Struct. **30**, 3 (2012).

[75] C. Kato, A. Iida, Y. Takano, H. Fujita, and M. Ikegawa, Numerical prediction of aerodynamic noise radiated from low mach number turbulent wake, in *Proceedings of the 31st Aerospace Sciences Meeting* (AIAA, Reston, VA, 1993), AIAA paper 1993–145.